

Direct observation of cycloidal spin modulation and field-induced transition in Néel-type skyrmion-hosting VOSe_2O_5

T. Kurumaji^{1*}, T. Nakajima^{1†}, A. Feoktystov², E. Babcock², Z. Salhi², V. Ukleev^{1,3},

T. Arima^{1,4}, K. Kakurai^{1,5}, and Y. Tokura^{1,6}

¹ *RIKEN Center for Emergent Matter Science (CEMS), Wako 351-0198, Japan,*

² *Forschungszentrum Jülich GmbH, Jülich Center for Neutron Science (JCNS) at Heinz Maier-Leibnitz Zentrum (MLZ), Garching 85748, Germany,*

³ *Laboratory for Neutron Scattering and Imaging (LNS), Paul Scherrer Institute (PSI), CH-5232 Villigen, Switzerland,*

⁴ *Department of Advanced Materials Science, The University of Tokyo, Kashiwa 277-8561, Japan,*

⁵ *CROSS-Tokai, Research Center for Neutron Science and Technology, Tokai, Ibaraki 319-1106, Japan,*

⁶ *Department of Applied Physics, The University of Tokyo, Tokyo 113-8656, Japan.*

*Current address: Department of Physics, Massachusetts Institute of Technology, Cambridge, Massachusetts 02139, USA.

†Current address: Institute for Solid State Physics, The University of Tokyo, Chiba 277-8581, Japan.

Abstract

We investigate the spin rotational structure of magnetic skyrmions in a tetragonal polar magnet VOSe_2O_5 via polarized small-angle neutron scattering (SANS). Spin polarization analysis of the scattered neutrons reveals the cycloidal spin modulation in all the incommensurate phases at zero and non-zero magnetic field along the c axis, providing unambiguous evidence for Néel-type skyrmions in this system. In the vicinity of the triangular skyrmion-lattice phase, extensive SANS measurements unravel a field-induced spin texture renouncing square skyrmion-lattice state, suggesting the relevance of thermal fluctuations to the topology of spin textures in this polar magnet.

Magnetic domain walls (DW), chiral soliton-lattices, and skyrmions are spatially-varying noncollinear and/or noncoplanar arrangement of spins in magnets characterized by nontrivial winding number in 1D or 2D space [1-3]. These spin structures, when isolated in ferromagnetic background, can be viewed as a particle, and mobile via strong coupling with conduction electrons, hence being promising candidates for current-driven information carriers in spintronics devices [4,5]. These structures are characterized by spin helicity γ which represents how the magnetic moments are twisted with respect to the spatial coordinates [1]. Spin axes rotate in the plane parallel to the propagation vector (q vector) in a Néel-type DW/skyrmion with $\gamma = 0$, and π (Figs. 1(a, c)), which is in contrast with the Bloch-type spin configurations for $\gamma = \pm \frac{\pi}{2}$ (the signs define the handedness), where the spin rotation plane is perpendicular to the q vector (Figs. 1(b, d)). Recent studies have revealed a significant role of γ in the current-induced motion of DW/skyrmions through spin-orbit torques and spin-transfer torques [5-10]. These features provoke pressing interest in experimental techniques to determine γ of these topological spin solitons.

Since the discovery of skyrmion-lattice (SkL) state in chiral magnets [11,12], recent experimental efforts have revealed that various classes of materials including bulk compounds [13] and thin-films/heterostructures host skyrmions with different helicities as well as vorticities [14]. Internal degrees of freedom are mostly selected by Dzyaloshinskii-Moriya interaction [15,16] imprinted from the crystal structure with broken inversion symmetry. Recent studies have discovered that these materials harbor versatile magnetic

phase diagrams including both equilibrium and metastable skyrmions with different lattice forms such as triangular and square SkL states [17-21]. These rich features are generated from subtle balance among thermal fluctuations, Zeeman energy, magnetic anisotropy, and perhaps multi-spin exchange interactions [17,22-26]. Development of widely applicable methods to determine the spin configurations as well as the SkL form is essential for understanding the link among spin textures and their stability.

In order to determine the orientations of the magnetic moments composing skyrmions and to monitor the phase transitions in external fields, multiple experimental techniques are available, including Lorentz transmitting electron microscopy (LTEM) [12,27,28], spin polarized scanning tunneling microscopy (SPSTM) [17,29], spin-polarized low-energy electron microscopy (SPLEEM) [30], nitrogen-vacancy (NV) center based microscopy [31,32], and circular-dichroism in magnetic x-ray scattering [33,34]. Although LTEM has been well established to detect Bloch-type DW/skyrmions, it has only a limited sensitivity to Néel-type configuration due to geometrical condition for the electron beam with respect to magnetic moments [27,28]. The other techniques have been proved effective to distinguish the types of skyrmions and their helicities while they are mostly available at, or sensitive to the surfaces of specimens.

We here focus on polarized small-angle neutron scattering (PSANS), which distinguishes the helicity of spin textures, and is broadly applicable to monitor the magnetic phase transitions in bulk compounds [35]. Up to now, Bloch-type magnetic modulations in magnetic fields were partly confirmed in the previous study with MnSi [36]. As for Néel-

type skyrmions, previous PSANS study in polar GaV_4S_8 [37] reported the evidence of cycloidal spin modulation in magnetic phases, while the intensity for skyrmions is hard to separate from that for the multi-domain state of the single- q cycloidal phase. Direct observation of Néel-type skyrmions via PSANS has remained to be established.

In this paper, we report the PSANS observation of the triangular-lattice state of the Néel-type skyrmion in VOSe_2O_5 . This material forms a square lattice of magnetic vanadium ions (V^{4+} ; $S = 1/2$) (Fig. 1(e)) belonging to a unique tetragonal polar group (space group: $P4cc$) [38-40], and has recently been identified to host the SkL state via unpolarized SANS [41]. Magnetic phase diagram for the magnetic field (H) along the c axis is reproduced in Fig. 1(f), which contains incommensurate spin states for cycloid (IC-1), triangular SkL (A), and IC-2 states together with paramagnetic (PM) and field-induced ferrimagnetic (FM) states. The spin structure for IC-2 state was provisionally assigned to the square SkL state based on the theories [22,23] and the observed four-fold SANS pattern in terms of the in-plane magnetic modulation [41]. We performed further experiment to address this hypothesis, and find that the square SkL is to be excluded, instead, an anisotropic double- q [22,42] structure is newly proposed here. The mechanism to stabilize this spin texture is also discussed.

Polarized and unpolarized SANS measurements were performed at KWS-1 with the previously used assembled single crystals [41]. Here, we introduce a Cartesian coordinate xyz as shown in the schematic experimental configuration of Fig. 1(g). The sample was mounted in a closed-cycle ^4He refrigerator, so that the crystallographic a , b , and c axes

were parallel to the x , y , and z axes, respectively. An incident spin-polarized neutron beam was obtained by a supermirror polarizer. The direction of incident neutron spins was controlled to be parallel or antiparallel to the z axis by a spin flipper, and was maintained by guide fields. The wavelength of the incident neutron beam was tuned to 10 Å. We employed polarized ^3He spin filter to analyze the spin-flip (SF) and non-spin-flip (NSF) scattering [43,44]. Flipping ratio and transmission were 20 to 15 % and 17 to 9 % at maximum to minimum, respectively. The decay time of the ^3He cells used was approximately 100 hours, which was monitored through the transmission of the direct neutron beam. Two different cells were used, J1 and Puck, which contain 5.2 and 5.0 bar cm of ^3He , respectively [45,46]. To extract the magnetic correlations below $T_C = 7.5$ K, the spectrum measured above T_C , typically at 8 K, was chosen as background. Imperfection of beam polarization was measured periodically and corrected following Refs. [47,48]. The H on the sample was produced by a Helmholtz coil.

Here, we describe the spatially-modulated magnetization with a wave vector \mathbf{q} as $\mathbf{m}(\mathbf{r}) = \text{Re}[\mathbf{m}_0 e^{i\mathbf{q}\cdot\mathbf{r}}]$ (\mathbf{m}_0 is a complex vector). In SANS, magnetic Bragg reflections appear when the scattering vector \mathbf{Q} ($= \mathbf{k}_i - \mathbf{k}_f$) coincides with the \mathbf{q} . Intensities of the magnetic reflections in the NSF (I_{NSF}), and SF (I_{SF}) channels are given by [49]

$$I_{\text{NSF}} = I_{\text{NSF}}^{++} + I_{\text{NSF}}^{--} \propto |m_z^\perp(\mathbf{Q})|^2, \quad (1)$$

$$I_{\text{SF}} = I_{\text{SF}}^{+-} + I_{\text{SF}}^{-+} \propto |m_x^\perp(\mathbf{Q}) + im_y^\perp(\mathbf{Q})|^2 + |m_x^\perp(\mathbf{Q}) - im_y^\perp(\mathbf{Q})|^2. \quad (2)$$

Here, we define $\mathbf{m}(\mathbf{Q})$ as the Fourier transformation of the $\mathbf{m}(\mathbf{r})$ and $\mathbf{m}^\perp(\mathbf{Q})$ as the projection on the plane perpendicular to the \mathbf{Q} , i.e., $\mathbf{m}^\perp(\mathbf{Q}) = \mathbf{m}(\mathbf{Q}) - [\mathbf{m}(\mathbf{Q}) \cdot \hat{\mathbf{Q}}]\hat{\mathbf{Q}}$, where $\hat{\mathbf{Q}}$ is the unit vector parallel to \mathbf{Q} . The unified expression for the cycloidal and proper-screw spin configurations propagating along the x axis (Figs. 1(a,b)) is given by

$$\mathbf{m}(\mathbf{r}) = m_z \cos(qx) \hat{\mathbf{z}} + (m_x \cos \gamma \hat{\mathbf{x}} + m_y \sin \gamma \hat{\mathbf{y}}) \sin(qx). \quad (3)$$

Note that the m_x component does not contribute to $\mathbf{m}^\perp(\mathbf{Q})$. By substituting Eq. (3) into Eqs. (1) and (2), one can find that the difference between cycloidal and proper-screw spin configurations are clearly seen in the I_{SF} , which is absent in the former, but present in the latter. NSF channel is produced by the m_z component, and present in both cases [50]. These relationships are available to determine the type of helicity of a SkL state, which is described by the superposition of q vectors in the plane perpendicular to the neutron beam.

Figures 2(a) and 2(b) show the observed NSF and SF scattering, respectively, for the triangular SkL state in the A phase. Presence of intensity in NSF channel (Fig. 2(a)) and absence of that in SF channel (Fig. 2(b)) provide clear evidence for the Néel-type skyrmion state with $\gamma = 0$ or π [51]. We also confirmed that the NSF channel reproduces the twelve-fold intensity peaks at $|q| = 0.048 \text{ nm}^{-1}$ as observed in Ref. [41]. This is due to the coexistence of two domains of triangular SkL state with one of the q vectors locked along either a or b axis (Fig. 2(g)). This feature enables us to observe the skyrmion state in the present system separably from the single- q cycloidal state, which produces four-fold Bragg peaks (Fig. 2(c)). As for GaV_4S_8 [37], on the other hand, the SANS intensity for the

skyrmion state isotropically distributes for the q vector in the plane perpendicular to the trigonal crystal axes to form a ring-like scattering pattern. Due to this situation, it was difficult to exclude the possibility of the multidomain of cycloidal state by the PSANS measurement alone. Note that the observation of the NSF channel in the A phase indicates the m_z component, excluding the multiple- q state with spins lying in the ab -plane such as being recently reported for polar YCo_8Sn_4 [52].

We also determined the type of helicity of the spin modulations in the IC-1, and IC-2 state. Figure 2(c) shows the intensity pattern for the NSF channel in the IC-1 state, reproducing that in the unpolarized SANS study [41], i.e., four-fold peaks for $q\parallel a^*$ and $q\parallel b^*$ superposed with weak ring-like intensity due to diffusive q -domains. This indicates that two kinds of domain with q_a and q_b dominates as shown in Fig. 2(h). Absence of the intensity in the SF channel (Fig. 2(d)) confirms the cycloidal spin configuration in the IC-1 state as assigned in Ref. [41]. We also proved the cycloidal spin configuration in the IC-2 state by the presence and absence of the PSANS intensity for NSF (Fig. 2(e)) and SF channel (Fig. 2(f)), respectively. The IC-2 state was previously proposed as the square-lattice of the Néel-type skyrmions. This hypothetical spin texture is expressed by the equivalent superposition of two cycloidal spin modulations propagating along a and b axes, respectively. We did not confirm whether the magnitude of these two modulations are equivalent or contain some sort of anisotropy because the possible multidomain state of the latter would be indistinguishable from the former. In the latter case, the spin texture is not the square SkL state, but is rather termed an anisotropic double- q state proposed in

theoretical works [22,42]. Schematic multidomain configuration is depicted in Fig. 2(i). Diffusive q -domains as observed by the ring-like pattern in Fig. 2(e) are not shown here.

In order to investigate the multiple- q nature for the IC-2 phase, we monitor the field dependence of the unpolarized SANS intensity through the phase transition from IC-1 state to IC-2 state for $H||c$ at $T = 6.67$ K. Prior to the measurement, we rotated the Helmholtz coil in the horizontal (zx) plane to apply H along the x (a) axis. The single domain of the IC-1 state with $q||b^*$ (Fig. 3(a)) was selected due to the anisotropy of the Zeeman energy for the cycloidal spin configuration [41]. After eliminating the H , we rotated the coil back to $H||z(c)$ configuration. We subsequently applied the field along the c axis to take the minor loop as shown in Figs. 3(a)-(h). We find that even at $\mu_0 H = 5$ and 6 mT (Figs. 3(c-d)), in the center of the IC-2 phase (Fig. 1(f)), the SANS intensity for $q||a^*$ remains considerably weaker than that for $q||b^*$. This excludes the formation of the square SkL state in the IC-2 phase. We note that at the end of the minor loop (Fig. 3(h), $\mu_0 H = 0$ mT) the intensity for $q||a^*$ shows up, suggesting the multidomain formation for the IC-1 state.

For more quantitative perspective, we plotted the field dependence of the averaged wavelength λ ($= \frac{2\pi}{q}$) (Fig. 4(a)) and the integrated intensities for the respective vertical and horizontal areas (Fig. 4(b)). As increasing the field, λ increases and shows a kink at around 2.5 mT signaling the transition into the IC-2 state. We find that λ shows a hysteresis in the backward scan for the minor loop (open symbols in Fig. 4(a)) only in the IC-2 region. This reflects the different spin textures in IC-1 and IC-2 state separated by a

first-order phase boundary. Furthermore, the intensity for the horizontal direction ($q||a^*$) appears in the IC-2 state as shown in Fig. 4(b). This feature for the IC-2 state is hard to be reconciled with the single- q model as the IC-1 state.

Here, we propose an anisotropic double- q state for the spin structure of the IC-2 state. This was initially proposed as a stable spin texture in a chiral magnet with tetragonal single-site anisotropy and/or compass-type anisotropic exchange interaction [22,42]. The spin density $\mathbf{S}(x, y)$ is expressed as

$$\mathbf{S}(x, y) = C_x(\sin qx, 0, \cos qx) + C_y(0, \cos qy, \sin qy), \quad (4)$$

where the amplitudes for the cycloidal modulations along x and y axes are different with each other ($C_x \neq C_y$). On the basis of this spin structure model, we can describe the evolution of the intensity in the minor loop as schematically illustrated in Fig. 4(c). Starting from the purified single-domain of the IC-1 state (1) with q_b in zero field, the intensity for the minor q_a modulation develops with $H||c$ (2) due to the formation of the IC-2 state with the primal q_b . Further increase of the field induces the FM state (3) at some parts of the pieces of crystals erasing the memory of the q orientation. In the backward scan, the region for the FM state returns to the IC-2 state (4) with randomly selecting the primal q vectors, which is compatible with the observation where the intensities for $q||a^*$ and $q||b^*$ evolve parallel with each other (open symbols in Fig. 4(b)). Inequality of these intensities can be ascribed to the remnant domain for the IC-2 state, which does not lose the memory from the initial single domain state. Eventually, the system comes back to the

IC-1 state (5) in zero field with contamination of the domain with q_a , as observed in Fig. 3(h).

The anisotropic double- q model can qualitatively explain the observation as mentioned above, while we point out a deviation from the theories [22,42], where the double- q state is predicted to continuously connect to zero field. The IC-2 state is stable only in a non-zero field (Fig. 1(f)). We hypothesize that this difference would originate from the thermal fluctuations, which were not considered in the previous theoretical studies. Square SkL state is supposed to position, if present, at relatively low temperatures from the fact that the corresponding square lattice states of the Bloch-type skyrmions have been observed only as the metastable state close to the zero temperature [19,20] or thermodynamically stable only at low temperatures [21]. In VOSe_2O_5 , on the other hand, easy-plane type anisotropy destabilizes the spin modulation below 4 K [41]; this perhaps makes the square SkL state difficult to form in the present compound. To clarify this point, further theoretical investigation considering a delicate effect of thermal fluctuations would be desirable.

In conclusion, we directly determined the orientation of the magnetic moments composing of the SkL state via PSANS measurement to confirm the Néel-type skyrmions in the tetragonal polar magnet VOSe_2O_5 . We also obtained the evidence that the spin configuration for the other modulated magnetic phases surrounding the SkL phase, i.e., the IC-1 and IC-2 states, are both described with the cycloidal modulations. On the basis of the field evolution of the SANS pattern from the IC-1 (single- q cycloid) to the IC-2 states, we proposed the anisotropic double- q state for the IC-2 phase. The present study provides

a useful guiding principle to apply this procedure to determination of complex or multiple helical modulations anticipated to occur in skyrmion-hosting materials.

References and Notes

1. A. Hubert, and R. Schäfer, *Magnetic Domains The analysis of magnetic microstructures*, (Springer, 1998).
2. Y. Togawa, Y. Kousaka, K. Inoue, and J.-i. Kishine, *Symmetry, structure, and dynamics of monoaxial chiral magnets*, J. Phys. Soc. Jpn. **85**, 112001 (2016).
3. N. Nagaosa, and Y. Tokura, *Topological properties and dynamics of magnetic skyrmions*, Nat. Nanotech. **8**, 899 (2013).
4. A. Fert, V. Cros, and J. Sampaio, *Skyrmions on the track*, Nat. Nanotech. **8**, 152 (2013).
5. S. S. P. Parkin, M. Hayashi, and L. Thomas, *Magnetic domain-wall racetrack memory*, Science **320**, 190 (2008).
6. I. M. Miron, T. Moore, H. Szambolics, L. D. Buda-Prejbeanu, S. Auffret, B. Rodmacq, S. Pizzini, J. Vogel, M. Bonfim, A. Schuhl, and G. Gaudin, *Fast current-induced domain-wall motion controlled by the Rashba effect*, Nat. Mater. **10**, 419 (2011).
7. S. Emori, U. Bauer, S.-M. Ahn, E. Martinez, and G. S. D. Beach, *Current-driven dynamics of chiral ferromagnetic domain walls*, Nat. Mater. **12**, 611 (2013).
8. K.-S. Ryu, L. Thomas, S.-H. Yang, and S. Parkin, *Chiral spin torque at magnetic domain walls*, Nat. Nanotech. **8**, 527 (2013).
9. J. Sampaio, V. Cros, S. Rohart, A. Thiaville, and A. Fert, *Nucleation, stability and current-induced motion of isolated magnetic skyrmions in nanostructures*, Nat. Nanotech. **8**, 839 (2013).
10. S. Woo, K. Litzius, B. Krüger, M.-Y. Im, L. Caretta, K. Richter, M. Mann, A. Krone, R. M. Reeve, M. Weigand, P. Agrawal, I. Lemesch, M.-A. Mawass, P. Fischer, M. Kläui, and G. S. D. Beach, *Observation of room-temperature magnetic skyrmions and their current-driven dynamics in ultrathin metallic ferromagnets*, Nat. Mater. **15**, 501, (2016).
11. S. Mühlbauer, B. Binz, F. Jonietz, C. Pfleiderer, A. Rosch, A. Neubauer, R. Georgii, and P. Boni, *Skyrmion lattice in a chiral magnet*, Science **323**, 915 (2009).
12. X. Z. Yu, Y. Onose, N. Kanazawa, J. H. Park, J. H. Han, Y. Matsui, N. Nagaosa, and Y. Tokura, *Real-space observation of a two-dimensional skyrmion crystal*, Nature **465**, 901 (2010).
13. A. Bauer, and C. Pfleiderer, *Generic aspects of skyrmion lattices in chiral magnets*, (Springer International Publishing, 2016).

14. W. Jiang, G. Chen, K. Liu, J. Zang, S. G.E. te Velthuis, and A. Hoffmann, *Skyrmions in magnetic multilayers*, Phys. Rep. **704**, 1 (2017).
15. A. N. Bogdanov, and D. A. Yablonskii, *Thermodynamically stable “vortices” in magnetically ordered crystals. The mixed state of magnets*, Sov. Phys. JETP **68**, 101 (1989).
16. A. Bogdanov, and A. Hubert, *Thermodynamically stable magnetic vortex states in magnetic crystals*, J. Magn. Magn. Mat. **138**, 255 (1994).
17. S. Heinze, K. von Bergmann, M. Menzel, J. Brede, A. Kubetzka, R. Wiesendanger, G. Bihlmayer, and S. Blugel, *Spontaneous atomic-scale magnetic skyrmion lattice in two dimensions*, Nat. Phys. **7**, 713 (2011).
18. H. Oike, A. Kikkawa, N. Kanazawa, Y. Taguchi, M. Kawasaki, Y. Tokura, and F. Kagawa, *Interplay between topological and thermodynamic stability in a metastable magnetic skyrmion lattice*, Nat. Phys. **12**, 62 (2016).
19. K. Karube, J. S. White, N. Reynolds, J. L. Gavilano, H. Oike, A. Kikkawa, F. Kagawa, Y. Tokunaga, H. M. Rønnow, Y. Tokura, and Y. Taguchi, *Robust metastable skyrmions and their triangular-square lattice structural transition in a high-temperature chiral magnet*, Nat. Mater. **15**, 1237 (2016).
20. T. Nakajima, H. Oike, A. Kikkawa, E. P. Gilbert, N. Booth, K. Kakurai, Y. Taguchi, Y. Tokura, F. Kagawa, and T.-h. Arima, *Skyrmion lattice structural transition in MnSi*, Sci. Adv. **3**:e102562 (2017).
21. A. Chacon, L. Heinen, M. Halder, A. Bauer, W. Simeth, S. Mühlbauer, H. Berger, M. Garst, A. Rosch, and C. Pfleiderer, *Observation of two independent skyrmion phases in a chiral magnetic material*, Nat. Phys. **14**, 936 (2018).
22. S. D. Yi, S. Onoda, N. Nagaosa, and J. H. Han, *Skyrmions and anomalous Hall effect in a Dzyaloshinskii-Moriya spiral magnet*, Phys. Rev. B **80**, 054416 (2009).
23. J. Rowland, S. Banerjee, and M. Randeria, *Skyrmions in chiral magnets with Rashba and Dresselhaus spin-orbit coupling*, Phys. Rev. B **93**, 020404(R) (2016).
24. T. Okubo, S. Chung, and H. Kawamura, *Multiple- q states and the skyrmion lattice of the triangular-lattice Heisenberg antiferromagnet under magnetic field*, Phys. Rev. Lett. **108**, 017206 (2012).
25. A. O. Leonov, and M. Mostovoy, *Multiply periodic states and isolated skyrmions in an anisotropic frustrated magnet*, Nat. Commun. **6**, 8275 (2015).

26. S. Hayami, R. Ozawa, and Y. Motome, *Effective bilinear-biquadratic model for noncoplanar ordering in itinerant magnets*, Phys. Rev. B **95**, 224424 (2017).
27. S. D. Pollard, J. A. Garlow, J. Yu, Z. Wang, Y. Zhu, and H. Yang, *Observation of stable Néel skyrmions in cobalt/palladium multilayers with Lorentz transmission electron microscopy*, Nat. Commun. **8**, 14761 (2017).
28. J. A. Garlow, S. D. Pollard, M. Beleggia, T. Dutta, H. Yang, and Y. Zhu, *Quantification of mixed Bloch-Neel topological spin textures stabilized by the Dzyaloshinskii-Moriya interaction in Co/Pd multilayers*, Phys. Rev. Lett. **122**, 237201 (2019).
29. N. Romming, C. Hanneken, M. Menzel, J. E. Bickel, B. Wolter, K. von Bergmann, A. Kubetzka, and R. Wiesendanger, *Writing and deleting single magnetic skyrmions*, Science **341**, 636 (2013).
30. G. Chen, A. Mascaraque, A. T. N'Diaye, and A. K. Schmid, *Room temperature skyrmion ground state stabilized through interlayer exchange coupling*, Appl. Phys. Lett. **106**, 242404 (2015).
31. Y. Dovzhenko, F. Casola, S. Schlotter, T. X. Zhou, F. Buttner, R. L. Walsworth, G. S. D. Beach, and A. Yacoby, *Magnetostatic twists in room-temperature skyrmions explored by nitrogen-vacancy center spin texture reconstruction*, Nat. Commun. **9**, 2712 (2018).
32. J.-P. Tetienne, T. Hingant, L. J. Martinez, S. Rohart, A. Thiaville, L. H. Diez, K. Garcia, J.-P. Adam, J.-V. Kim, J.-F. Roch, I. M. Miron, G. Gaudin, L. Vila, B. Ocker, D. Ravelosona, and V. Jacques, *The nature of domain walls in ultrathin ferromagnets revealed by scanning nanomagnetometry*, Nat. Commun. **6**, 6733 (2015).
33. O. Boulle *et al.*, *Room-temperature chiral magnetic skyrmions in ultrathin magnetic nanostructures*, Nat. Nanotech. **11**, 449 (2016).
34. W. Legrand, J.-Y. Chauleau, D. Maccariello, N. Reyren, S. Collin, K. Bouzehouane, N. Jaouen, V. Cros, and A. Fert, *Hybrid chiral domain walls and skyrmions in magnetic multilayers*, Sci. Adv. **4**, eaat0415 (2018).
35. S. Mühlbauer, D. Honecker, É. A. Périgo, F. Bergner, S. Disch, A. Heinemann, S. Erokhin, D. Berkov, C. Leighton, M. R. Eskildsen, and A. Michels, *Magnetic small-angle neutron scattering*, Rev. Mod. Phys. **91**, 015004 (2019).
36. C. Pappas, E. Lelièvre-Berna, P. Falus, P. M. Bentley, E. Moskvin, S. Grigoriev, P. Fouquet, and B. Farago, *Chiral paramagnetic skyrmion-like phase in MnSi*, Phys. Rev. Lett. **102**, 197202 (2009).

37. J. S. White, Á. Butykai, R. Cubitt, D. Honecker, C. D. Dewhurst, L. F. Kiss, V. Tsurkan, and S. Bordács, *Direct evidence for cycloidal modulations in the thermal-fluctuation-stabilized spin spiral and skyrmion states of GaV₄S₈*, Phys. Rev. B **97**, 020401(R) (2018).
38. G. Meunier, M. Bertaud, and J. Galy, Acta Cryst. **B30**, 2834 (1974).
39. J.-C. Trombe, A. Gleizes, J. Galy, J.-P. Renard, Y. Journaux, and M. Verdaguer, Nouveau Journal De Chimie **11**, 321 (1987).
40. S.-H. Kim, P. S. Halasyamani, B. C. Melot, R. Seshadri, M. A. Green, A. S. Sefat, and D. Mandrus, *Experimental and computational investigation of the polar ferrimagnet VOSe₂O₅*, Chem. Mater. **22**, 5074 (2010).
41. T. Kurumaji, T. Nakajima, V. Ukleev, A. Feoktystov, T.-h. Arima, K. Kakurai, and Y. Tokura, *Néel-type skyrmion lattice in the tetragonal polar magnet VOSe₂O₅*, Phys. Rev. Lett. **119**, 237201 (2017).
42. J. P. Chen, D.-W. Zhang, and J.-M. Liu, *Exotic skyrmion crystals in chiral magnets with compass anisotropy*, Sci. Rep. **6**, 29126 (2016).
43. A. V. Feoktystov, H. Frielinghaus, Z. Di, S. Jaksch, V. Pipich, M.-S. Appavou, E. Babcock, R. Hanslik, R. Engels, G. Kemmerling, H. Kleines, A. Ioffe, D. Richter, and T. Brückel, *KWS-1 high-resolution small-angle neutron scattering instrument at JCNS: current state*, J. Appl. Cryst. **48**, 61 (2015).
44. E. Babcock, Z. Salhi, T. Theisselmann, D. Starostin, J. Schmeissner, A. Feoktystov, S. Mattauch, P. Pistel, A. Radulescu, and A. Ioffe, *SEOP polarized ³He neutron spin filters for the JCNS user program*, J. Phys.: Conf. Ser. **711**, 012008 (2016).
45. S. R. Parnell, E. Babcock, K. Nünighoff, M. W. A. Skoda, S. Boag, S. Masalovich, W. C. Chen, R. Georgii, J. M. Wild, C. D. Frost, *Study of spin-exchange optically pumped ³He cells with high polarization and long lifetimes*, Nucl. Instr. and Meth. A **598**, 774 (2009).
46. Z. Salhi, E. Babcock, P. Pistel, and A. Ioffe, *³He neutron spin filter cell development program at JCNS*, J. Phys.: Conf. Ser. **528**, 012015 (2014).
47. A. R. Wildes, *Scientific reviews: neutron polarization analysis corrections made easy*, Neutron News **17**, 17 (2006).
48. E. Babcock, Z. Salhi, E. Kentzinger, S. Mattauch, and A. Ioffe, *Discussion on data correction for polarization analysis with a ³He spin filter analyzer*, J. Phys.: Conf. Ser. **862**, 012001 (2017).

49. R. M. Moon, T. Riste, and W. C. Koehler, *Polarization analysis of thermal-neutron scattering*, Phys. Rev. **181**, 920 (1969).
50. The present experiment lacks in sensitivity for the sign of the helicity (handedness).
51. The intensity around $q \sim 0$ for the SF channel (Fig. 2(b)) remains elusive. We suggest that this is due to either the spin structure with longer length scale or reflects the surface magnetic moments on the sample crystals.
52. R. Takagi, J. S. White, S. Hayami, R. Arita, D. Honecker, H. M. Rønnow, Y. Tokura, and S. Seki, *Multiple- q noncollinear magnetism in an itinerant hexagonal magnet*, Sci. Adv. **4**, eaau3402 (2018).

Acknowledgments

This research was supported in part by Grant-In-Aid for Young Scientists(B) No. 17K14351 from the Japan Society for the Promotion of Science (JSPS), and CREST No. JPMJCR1874 from the Japan Science and Technology Agency (JST).

Figure Captions

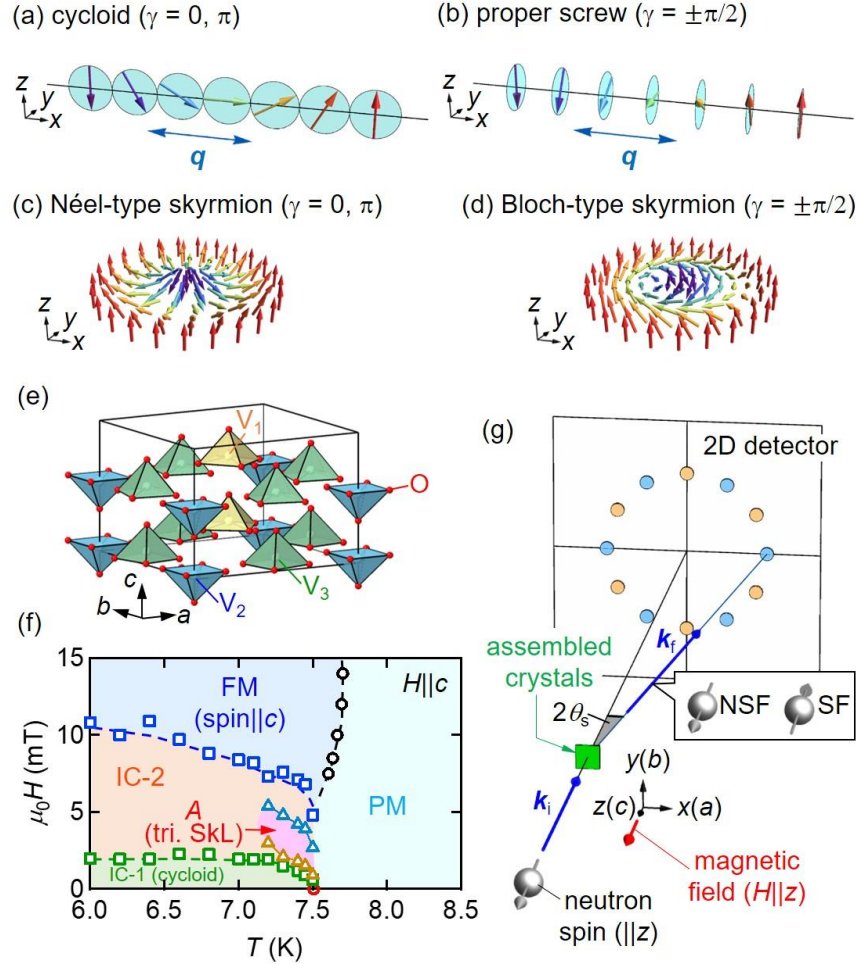


Fig. 1[(a) [(b)] Schematic cycloidal [proper screw] spin configuration. Helicity γ is decided by the spin rotation direction with respect to the q vector (see Eq. (3)). (c) [(d)] Spin configuration in a Néel- [Bloch]-type skyrmion. (e) Crystal structure of VOSe_2O_5 . Yellow, blue, and green tetragonal pyramids highlight respective VO_5 polyhedra. $\text{Se}_2\text{O}_5^{2-}$ molecular anions are not shown. (f) H - T phase diagram for assembled coaligned single crystals in $H||c$, reproduced from Ref. [41]. (g) Schematic PSANS setup used in the present study. The assembled crystals (green rectangle) are oriented with the c axis parallel to the incident

neutron beam direction (\mathbf{k}_i), and the z axis for the laboratory coordinate system. The H (red arrow) is applied along the z axis except for the field-trained process for the experiment focusing on the IC-2 state (see text). Neutron spin (gray arrow) is polarized along the z axis. $2\theta_s$ defines the scattering angle between \mathbf{k}_i and one of the final beam directions (\mathbf{k}_f) scattered by a modulation of spins. Blue and orange spots on the 2D detector indicate the doubling of six-fold magnetic Bragg peaks, for the domains of triangular SkL state with one of the triple- q vectors oriented along a and b axes, respectively.

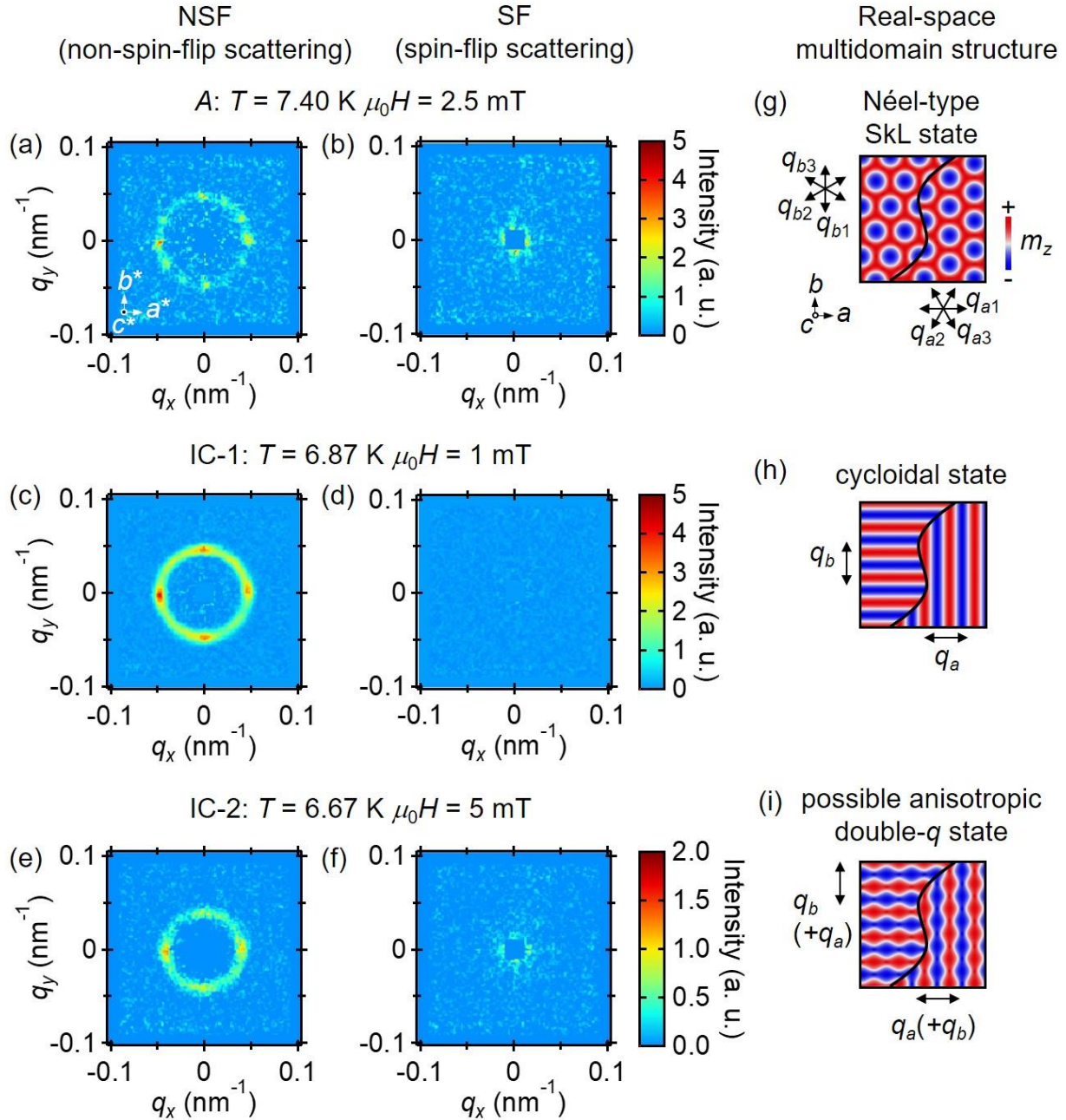


Fig. 2|(a), (c), (e) PSANS patterns of NSF and (b), (d), (f) SF channel at each magnetic phase. (a)-(b): A phase. (c)-(d): IC-1 phase. (e)-(f): IC-2 phase. (g)-(i) Color plot of m_z component for the schematic multidomain state of each magnetic phase. Black arrows indicate crystal axes or principal q -vectors for the spin structure in each domain. (g)

Triangular SkL state, (h) cycloidal state, and (i) anisotropic double- q state described by Eq. (4) as a candidate spin state for the IC-2 phase (see text).

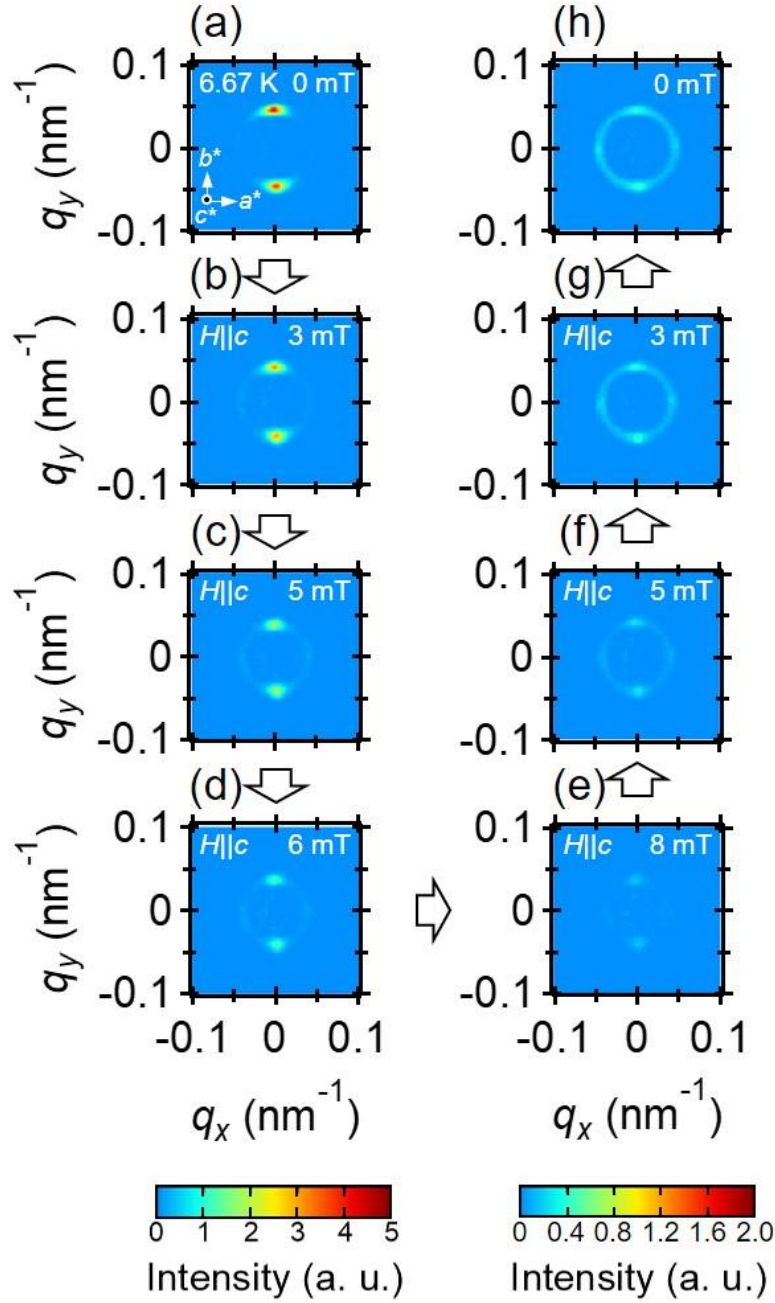


Fig. 3(a)-(h) Variation of SANS patterns at 6.67 K with $H||c$. The H changes from (a) 0 mT to (e) 8 mT and back to (h) 0 mT in the sequential order indicated by white arrows.

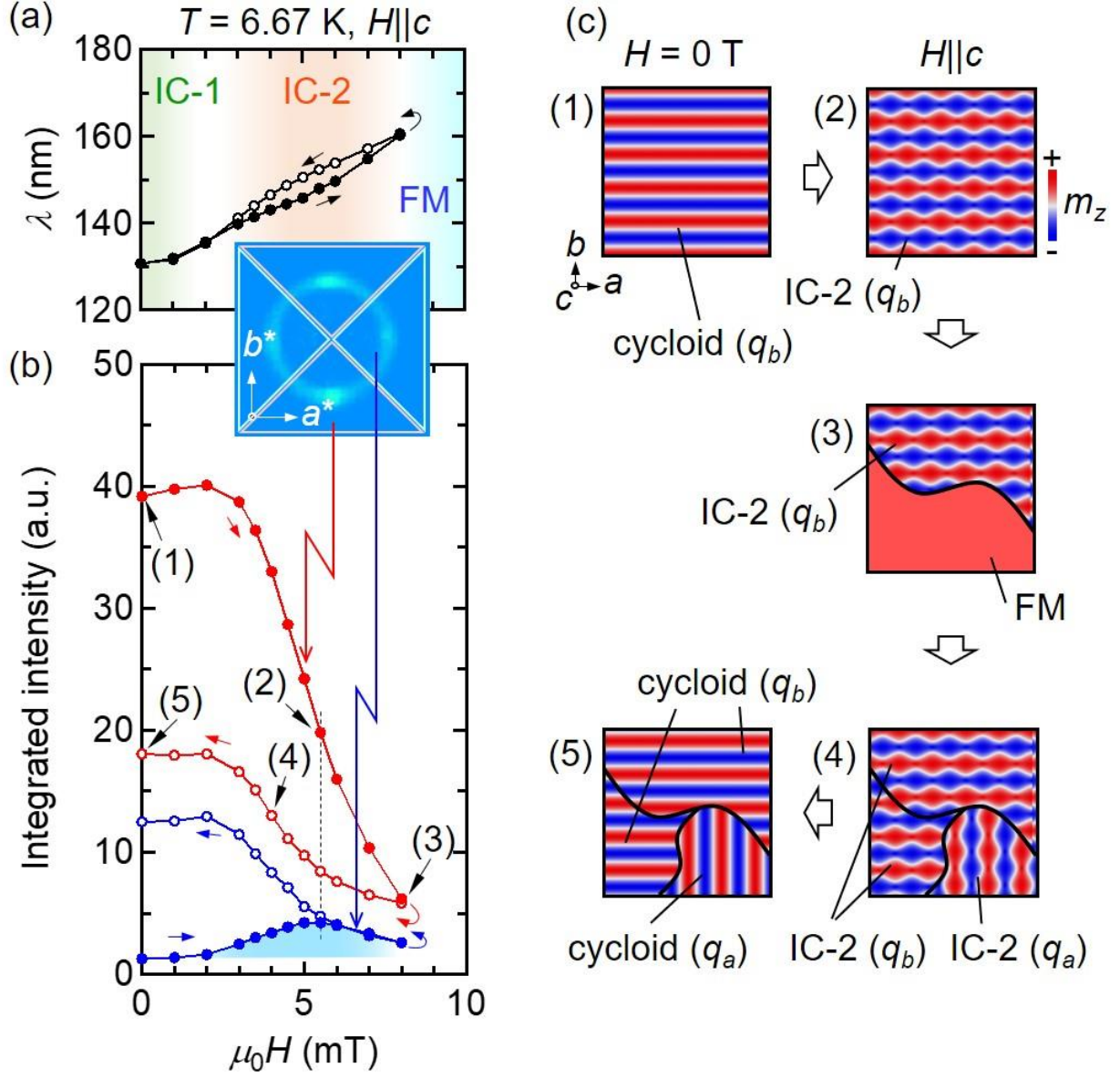


Fig. 4| (a)-(b) Magnetic-field dependence of (a) magnetic modulation wavelength (λ) and (b) integrated SANS intensities at 6.67 K in $H \parallel c$. Red (blue) circles are intensities for the vertical (horizontal) region as indicated in the inset. Closed (open) circles are for the H -increasing (decreasing) scan. (c) Schematic magnetic domain structure in the field-scan process along the minor loop from (1) to (5) as indicated in (b).